IOP Publishing Classical and Quantum Gravity
Class. Quantum Grav. **37** (2020) 065005 (16pp) https://doi.org/10.1088/1361-6382/ab6adf

Optical alignment and wavefront error demonstration of a prototype LISA telescope

Shannon R Sankar[1,3] **and Jeffrey Livas**[2]

[1] Department of Astronomy, University of Maryland, College Park, Greenbelt, MD, United States of America
[2] National Aeronautics and Space Administration, Goddard Space Flight Center, Greenbelt, MD, United States of America

E-mail: shannon.r.sankar@nasa.gov

Received 24 September 2019, revised 29 December 2019
Accepted for publication 13 January 2020
Published 18 February 2020

Abstract

In this work, we document the first complete alignment of a subscale prototype telescope for the LISA mission. An optical wavefront error map, which meets current mission requirements, was attained using alignment techniques consistent with production of multiple identical copies of a telescope for flight. We find that the telescope wavefront error is dominated by the as-built surface figure error of the mirrors and not the residual design wavefront error of the telescope prescription. Furthermore, this work shows the ability to implement a wavefront error allocation specific to the LISA telescope, lending confidence to such allocations for future flight telescopes, and provides a verified reference point for ongoing research into many aspects of the LISA optical system.

Keywords: LISA, laser interferometer space antenna, gravitational waves, telescope, interferometry

(Some figures may appear in colour only in the online journal)

1. Gravitational waves: the laser interferometer space antenna

Gravitational waves are propagating perturbations in spacetime, which had long been predicted by Einstein's general relativity. Only in the past few years have they been finally directly observed: the ground-based laser interferometer gravitational-wave observatory (LIGO) has now detected and studied gravitational waves from several sources including, for example, coalescing binary black holes [1] and merging neutron stars [2].

[3] Author to whom any correspondence should be addressed.

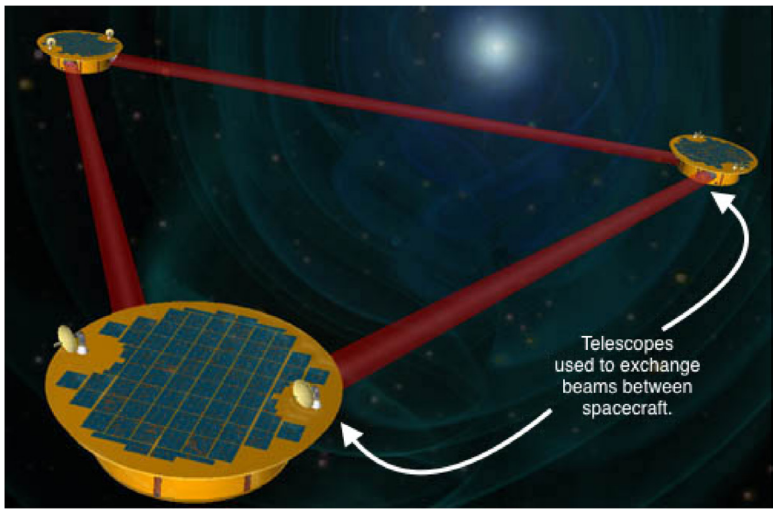

Figure 1. LISA performs interferometry between spacecraft separated by millions of kilometers. Telescopes located on each spacecraft simultaneously send and receive laser light. Image credit: NASA circa 2009. Not to scale.

LISA, the Laser Interferometer Space Antenna [3], is a space mission led by the European Space Agency (ESA) with substantial participation from the National Aeronautics and Space Administration (NASA). Currently scheduled to launch in 2034, as the third large class mission in ESA's Cosmic Vision Science Programme, LISA complements the science obtained from LIGO by observing gravitational waves in a frequency band where there are many expected gravitational wave sources but where ground-based observatories suffer from many sources of terrestrial noise. This LISA frequency band[4], which extends from 0.1 mHz to 0.1 Hz, houses a plethora of interesting astrophysical sources [4, 5]. These anticipated sources include (but are not limited to) binary coalescences of supermassive black holes with masses of 10^5–10^7 solar masses, intermediate mass black hole binaries of 10^2–10^5 solar masses and extreme mass ratio inspirals such as a 10 solar mass compact object falling into a 10^6 solar mass black hole [6–9].

LISA consists of three identical spacecraft orbiting a common point which trails the Earth by approximately 20° in a heliocentric orbit. The three spacecraft are separated from each other by distances of approximately 2.5 million kilometers. Laser links over these large distances allow precision interferometry of the inter-spacecraft displacement, one vital component of the observatory's gravitational wave science signal. An illustrative depiction of this constellation is shown in figure 1. Each spacecraft sends laser beams to—and receives laser beams from—both its sister spacecraft via specially-designed telescopes. The telescopes serve as afocal beam expanders and reducers, and limit the substantial optical diffraction loss experienced by the light in the inter-spacecraft arms of the triangular constellation. In total, six flight telescopes (two per spacecraft) are required, with the possibility of several other such telescopes being used for ground tests and as flight spares.

Research and development work for these telescopes has been initiated at NASA, including the development of design and analysis architectures as well as a hardware prototype telescope. This prototype studies many of the important optical characteristics required by flight

[4] The current LISA observatory sensitivity requirement extends from 0.1 mHz to 0.1 Hz, with a goal of 20 μHz–1 Hz.

models, and is the main subject of this work. One significant outcome of the studies involving this prototype telescope is the development of understanding into the alignment process. Since LISA requires six flight telescopes, this knowledge serves to improve both the realism of the alignment schedule and the confidence that the requirement can be successfully met.

1.1. Telescopes for LISA

The six LISA flight telescopes play a key role in enabling the mission's long arm interferometry, and so have several stringent requirements flowing directly down from the observatory science requirements. These telescope requirements include high dimensional stability, low backscattered light, high optical throughput, and low tilt-to-length coupling as discussed in [3]. The optical requirement specifications of the prototype are detailed in [10–12]. As is common in early phases of any space mission, many of these specifications will change as development towards flight occurs. However, several of the specifications—including the top level optical wavefront error allocation—have not changed significantly thus far. It is the wavefront error requirement that we chiefly address in this work.

The root-mean-square wavefront error is an often used measure of the variation of a wavefront map from a perfectly uniform flat wavefront, and is usually presented in units of length. For a given wavefront map $W(x, y)$, the root-mean-square wavefront error σ over an aperture A is given by the relation

$$\sigma^2 = \frac{1}{A}\int_A W(x,y)^2 \mathrm{d}x\mathrm{d}y - \left(\frac{1}{A}\int_A W(x,y)\mathrm{d}x\mathrm{d}y\right)^2. \tag{1}$$

The telescope wavefront error plays a direct role in determining the observatory sensitivity through several different considerations. At the top level, the wavefront error specification for the optical beam that propagates between the spacecraft is set at $\lambda/20$, of which a sub-allocation of $\lambda/30$ is attributed to the telescope. The top level allocation serves to bound the power loss experienced by light sent between spacecraft since aberrations in the sent wavefront will diffract to large angles in the far-field, and thereby reduce the optical intensity at the location of the far spacecraft [13]. Excess power loss could lower the gravitational wave signal-to-noise in the long baseline science interferometer, which interferes a local beam with light from a distant spacecraft collected by the telescope. Relative to an unaberrated transmitted beam, the light intensity at the receive spacecraft is reduced by a factor of approximately 0.90, due to rms aberrations at the level of $\lambda/20$ in the send aperture [13].

In addition to this top-level wavefront error allocation, there are other effects that depend on the wavefront error. For example, in the science interferometer, wavefront distortions from the telescope are directly imparted onto the received beam and could therefore limit the interferometric overlap between the local and received beams. Reduction in the beam overlap would also lead to a reduction of the signal-to-noise with which gravitational waves are observed. Another major consideration of the effect of wavefront error on the observatory performance is the coupling between angular tilts of the spacecraft and the sensed wavefront mean phase. One example of this coupling mechanism is as follows: the telescope wavefront error partially determines the far-field intensity pattern and the far-field spatial phase distribution. Angular noise in the transmitting spacecraft scan the phase distribution across the receiving spacecraft, leading to a variation in the phase which is unrelated to, and could mask, gravitational wave signals [14–16]. Numerical Monte Carlo simulations have been performed to determine the sensitivity of the received wavefront phase to angular jitter of the sending aperture—for an

rms wavefront error of $\lambda/20$ in the send aperture, the magnitude of this sensitivity was 0.07 pm nrad^{-1} [14].

Using these considerations and others, system level wavefront error budgets [12, 13, 17] have consistently allocated a root-mean-square wavefront error of one-thirtieth of a wave at the 1064 nm mission wavelength, or roughly 35.5 nm. In this correspondence, we address the demonstration of this required wavefront error in a complete prototype telescope—verification of other specifications will be addressed in subsequent works.

As the mission development timeline progresses, it may prove to be necessary to bound the composition of the wavefront error due to observatory-level interferometric constraints—such as coupling between angular and longitudinal degrees of freedom in the long baseline arm. One possible implementation of a constraint on the wavefront composition would be, for example, bounding the magnitude of specific Zernike terms in the wavefront. However, these specifications are still immature at the present time and, as such, were not included in the prototype developed in this work, but are expected to be addressed in subsequent engineering design units along the telescope path-to-flight development plan. Further development of such specifications is ongoing [14–16].

1.2. Prototype telescope versus flight telescopes

Even with a nominal launch date of approximately 2034, much telescope development work has already been completed at NASA, including the design and fabrication of a sub-scale prototype telescope described in this work. This prototype, which serves as a stepping stone to an eventual flight unit, has several key similarities to the flight units but also some important differences. These differences are sometimes due to changes in mission parameters in the time since the prototype was commissioned, and not due to any particular technical issue.

Two notable differences are the primary clear aperture diameter and overall telescope magnification. While flight units will have a magnification of 134, with a primary clear aperture of 300 mm, the prototype discussed in this work has a relaxed magnification of 40 and a primary clear aperture of 200 mm. Flight telescopes will have to meet all telescope specifications simultaneously while this prototype was intended to be a testbed of specific facets of telescope development and so was not required to meet all flight requirements. As an example, in an effort to reduce cost, the prototype was not fabricated from materials consistent with meeting the dimensional stability requirements, nor was this mechanical support structure designed to be consistent with demonstrating on-orbit thermal performance requirements. Table 1 summarizes some important differences between the prototype telescope and eventual flight versions. Full prototype telescope requirements are presented in more detail in [10, 11].

This sub-scale prototype was constructed to be an initial testbed for optical sensitivities and alignment tolerances and procedures, as well as for tests of scattered light performance. Therefore, the optics were fabricated to perform as similarly as possible to an eventual full scale flight telescope, within cost and schedule constraints. To meet the telescope wavefront specification of 35.5 nm, an error budget breakdown was developed prior to prototype fabrication and is summarized in table 2.

1.3. The prototype implementation

The implementation of the prototype falls into two major categories: the optical implementation and the mechanical hardware implementation. The optical implementation consists of the optical prescription chosen for meeting the specifications of the prototype telescope, as

Table 1. This table outlines some notable differences between the sub-scale prototype telescope and the eventual flight units. The flight specifications listed here are based on current values, and may change as the mission approaches launch readiness and further analyses are performed. This list is intended to be illustrative but not exhaustive. The frequency dependence of the dimension stability constraint is given by the relation $U(f) = \sqrt{1 + (2\ \text{mHz}/f)^4}$.

Parameter	Prototype	Flight
Large pupil diameter (mm)	200	300
Large pupil description	Real	Virtual
Small pupil diameter (mm)	5	2.24
Magnification (derived from above)	40	134
Acquisition field of regard (μrad)	$\pm$200	$\pm$225
Wavefront composition	Unconstrained	TBD (future)
Dimensional stability constraints	None	1 pm/$\sqrt{\text{Hz}} \times U(f)$

Table 2. This table outlines an *a priori* error allocation for achieving the overall $\lambda/30$ wavefront error specification of the prototype telescope, corresponding to roughly 35.5 nm. Note that the contributions listed for each of the four telescope mirrors are included as the effective wavefront error contribution due to fabrication, and not the surface error of each optic—the wavefront error for a reflective surface at normal incidence is twice the surface error.

Source of error	Error (nm RMS)	Comment
Design residual	4	Property of the optical prescription
Primary mirror	20	Off-axis parabolic mirror
Secondary mirror	20	Aspheric mirror
Tertiary mirror	10	Spherical mirror
Quaternary mirror	10	Spherical mirror
Mounting	5	Deformations of mirrors from mounting
Alignment residual	5	Cross-coupling of compensators, etc.
Calibration reserve	9	Margin for calibration of return flat
Margin	10	Reserve allocation
Estimated total	35.3	Assumes uncorrelated errors

well as the as-built optical surface deformations of the optical elements. The hardware implementation is the mechanical structure for holding and positioning the mirrors with sufficient accuracy to achieve the optical specifications.

1.3.1. Optical design of the prototype telescope. The prototype telescope is a four element, off-axis all-reflective design consisting of a parabolic primary mirror, an aspheric secondary mirror, and spherical tertiary and quaternary mirrors. The optical layout is shown in figure 2. This design form was chosen for compactness, good back-scattered light performance and ease of manufacturability. This particular optical prescription is well-corrected, permitting only 3.91 nm of residual design wavefront error in the narrow 8 μrad science field of view. The contribution of the optical design to the telescope's overall wavefront error within the central

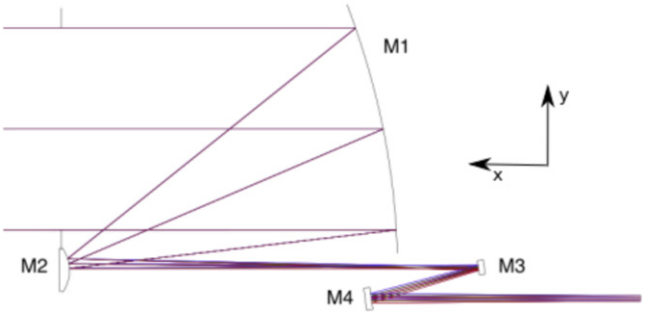

Figure 2. Optical layout of the prototype telescope. The primary, secondary, tertiary and quaternary mirrors are labelled M1, M2, M3 and M4 respectively.

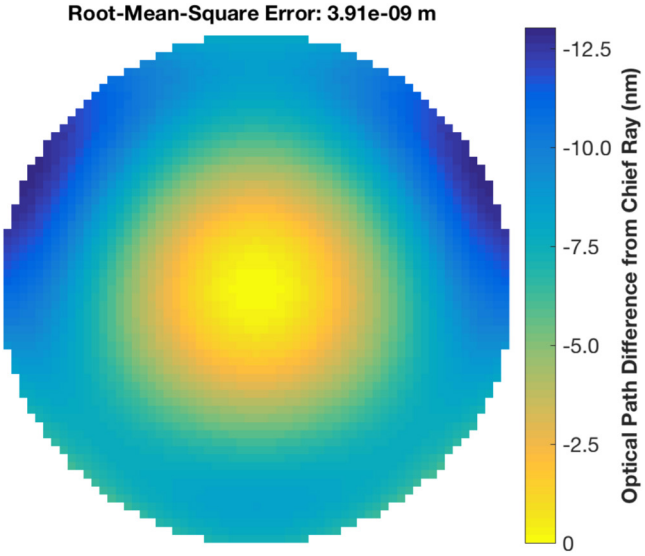

Figure 3. Design residual aberration of the prototype telescope expressed as an optical path difference from the chief ray in this center field.

science field of view is shown in figure 3. The residual aberration contribution of the optical design includes several terms, particularly defocus and primary spherical aberrations, but all terms were at a sufficiently low level to allow confidence that the as-built telescope would not be limited by the design.

1.3.2. As-built properties of the mirrors. A figure error allocation was made to each individual optic. This figure error budgeting enabled timely fabrication while still meeting the overall wavefront error goals of the telescope. Table 3 shows the chosen breakdown, as well as the surface figure error values obtained. Multiple copies of the physically smaller optics—the tertiary and quaternary mirrors—were fabricated and the achieved figures are all listed. Note that no limits were placed on any particular low order Zernike terms for these prototype mirrors. However, the mirrors were specified to have moderately low surface micro-roughness: 10 Å RMS for the primary and secondary mirrors, and 5 Å RMS for the tertiary and quaternary.

Table 3. Surface figure allocation made to each optic of the telescope. For the tertiary and quaternary mirrors, several copies were fabricated. Post-fabrication down-selection of suitable tertiary and quaternary mirrors was performed to meet the allocation, but the achieved surface figures for all the fabricated mirrors are listed for reference.

Mirror	Surface figure allocation (nm RMS)	Surface figure achieved (nm RMS)
Primary	$\leqslant$12	9.53
Secondary	$\leqslant$10	8.86
Tertiary	$\leqslant$5	3.82, 7.44, 4.83, 3.45, 4.74, 3.25, 3.40, 6.78, 2.91, 3.68
Quaternary	$\leqslant$5	2.79, 7.33, 3.72, 3.75, 1.78, 5.51, 6.39, 2.72, 3.43, 2.33

In combination with the low design residual wavefront error of 3.91 nm shown in figure 3, this breakdown enables a prototype telescope wavefront error of approximately 35 nm, meeting the telescope specification. It is key to note that the telescope, once assembled and aligned, therefore has a wavefront error dominated by the mirror surface figure errors, mainly from the primary and secondary mirrors. The low-to-mid spatial frequency figure errors on these mirrors are shown in figure 4.

After figuring the mirrors, optical coatings were applied. A complete set of mirrors—one primary mirror, one secondary mirror, and multiple tertiary and quaternary mirrors—were coated with low-loss, multi-layer dielectric coatings. These coatings were designed to have high reflectivity at the LISA laser wavelength of 1064 nm, but also sufficient reflectivity at 632 nm to enable testing using standard available instruments. A high precision spectrophotometer was used to quantify the multi-layer dielectric coatings and this data is presented in figure 5.

1.3.3. Physical hardware implementation of the prototype. The ability to achieve the design wavefront is partially governed by the ability to accurately and precisely position the mirrors, and the ability to compensate for unavoidable mirror manufacturing errors by re-positioning and aligning with real-time optical feedback. In addition to enabling the mirrors to be positioned correctly, another key property of the structure is the need to minimize the mount-induced mirror surface figure error, which includes both deformations of the mirror from mounting and sag of the mirror surface due to gravity. Furthermore, the physical implementation of the telescope allowed for ease of access for swapping out mirrors, especially for the tertiary and quaternary for which multiple mirror copies were fabricated.

The primary mirror of the prototype telescope was mounted in a three-point mounting structure. Clocking of the primary mirror in the mount was addressed by including reference points in the form of conical divots at the back of the mirror, near the center and the top. The top divot lines into a mounting screw, while the center divot can be used, for example, as a nest for alignment tooling balls.

The secondary mirror, which has the highest alignment sensitivity, is mounted into a holder which can be positioned by differential adjusters specifically built into the mounting structure. This method of having the positioners be a part of the metering structure provided a convenient option for placing and adjusting the mirror into alignment. However, in a flight telescope, such adjusters would be part of the ground support equipment—not part of the telescope metering structure—and removed before launch. For a flight telescope, the mirrors are likely to be placed using adjustable positioners, then permanently pinned or bonded in place [18] and, after curing, the adjusters would be removed before launch. However, for the prototype,

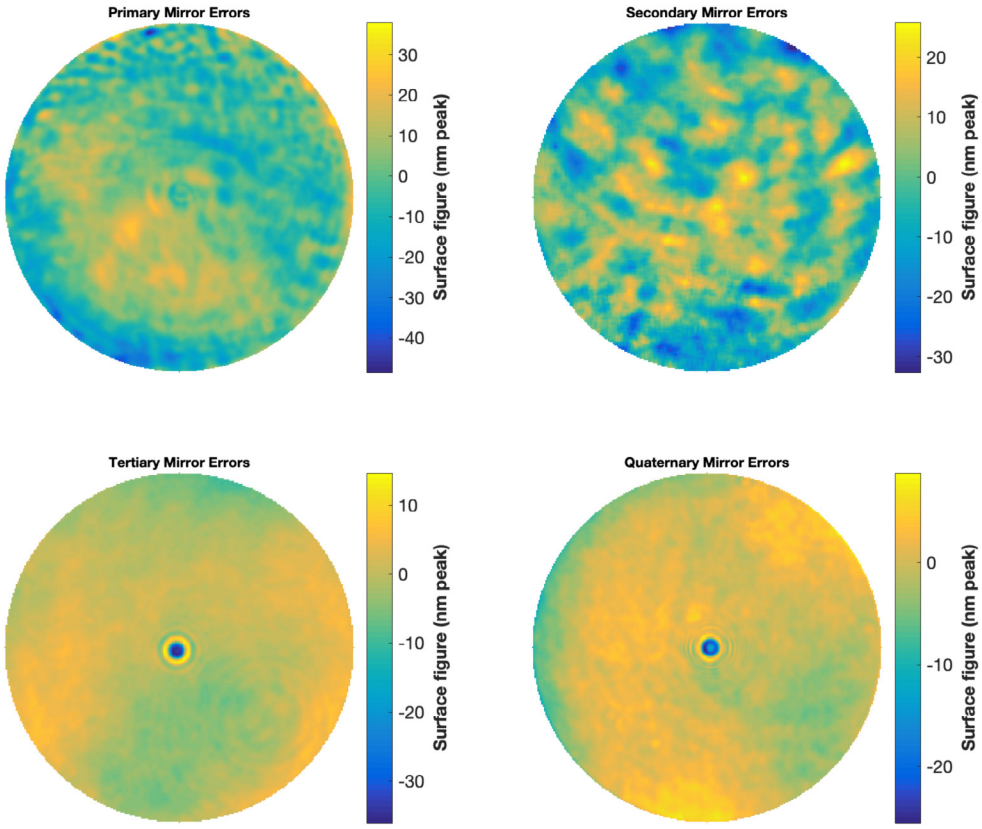

Figure 4. As-built surface figure errors of the four mirrors used in the prototype telescope. The coma aberration term clearly seen in the parabolic primary mirror and the central spots in the tertiary and quaternary mirror maps are artifacts of the surface figure measurement process. Only the first three Zernike terms—piston, tip and tilt—have been fit and removed from the above surface maps.

which was built in part to study alignment capabilities, having the adjusters as a part of the telescope structure was appropriate.

The wavefront error sensitivities of the tertiary and quaternary mirror positions in this optical design are low, especially when compensated by re-alignment of the secondary. Given these loose position tolerances, it was possible to position them using simple machining tolerances. These optics are mounted into holders which are aligned to a common structure using precision pins. This common structure is positioned using a separate metering block and simply bolted into place. An image of the physical implentation of the prototype is provided in figure 6.

The materials and construction techniques used in the prototype metering structure were chosen to keep the telescope wavefront error stable in a ± 3 K band about room temperature, and were not intended to provide the requisite LISA band dimensional stability expected in future flight units (see table 1).

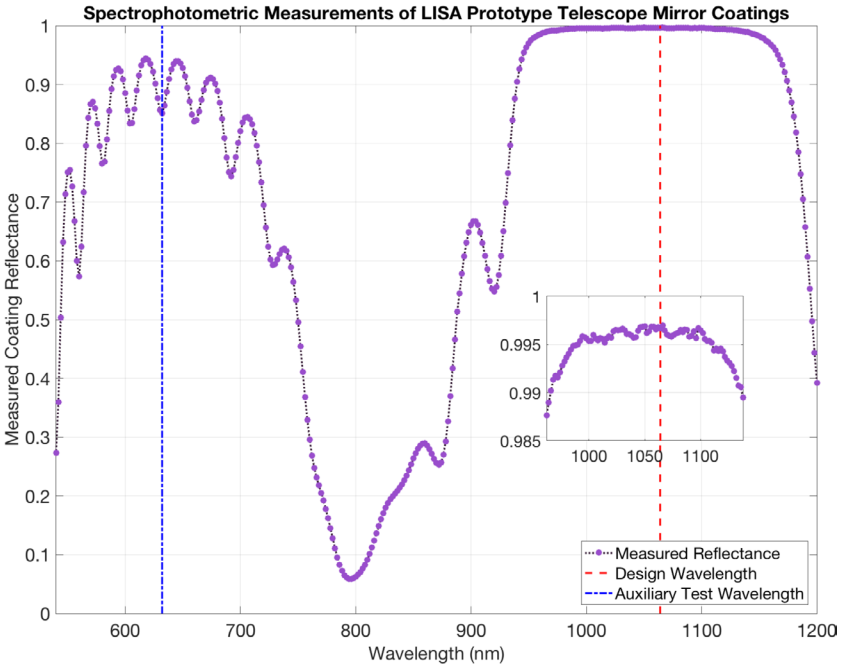

Figure 5. Spectrophotometer measurements of the dielectric coating applied to the optics. The inset shows a zoomed region near the LISA mission wavelength, showing that a reflectivity of greater than 0.995 was achieved at 1064 nm. High reflectivity over a wide band of wavelengths around 1064 nm compensates for the variation in the incident angles of the light for each of the four optics in the telescope.

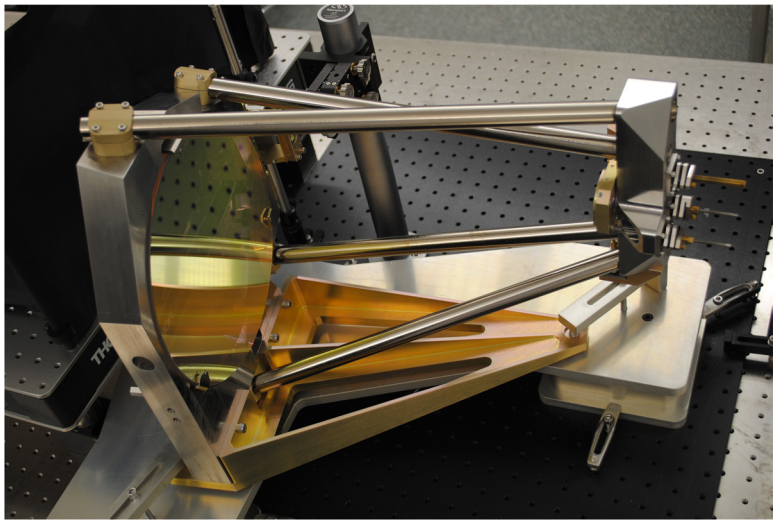

Figure 6. The physical prototype implementation in a cleanroom laboratory. Note the differential adjusters used to orient the secondary mirror for optical alignment.

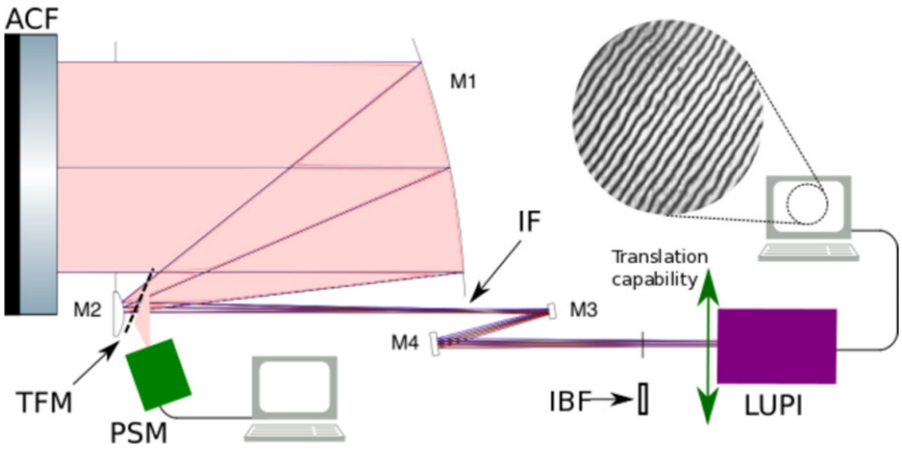

Figure 7. Diagram of the alignment process for the prototype telescope. The acronyms used are as follows. ACF: auto-collimating flat, TFM: temporary fold mirror, PSM: point-source microscope, IF: intermediate image, IBF: input beam flat, LUPI: laser unequal path interferometer. The primary, secondary, tertiary and quaternary mirrors of the telescope are referred to as M1, M2, M3 and M4, respectively. The ability to reliably translate the LUPI is shown in one direction—in reality translations in 5° of freedom are possible. A real interferogram from the alignment process is shown—several such interferograms were recorded, analyzed and averaged together as a form of mitigation against the effects of non-laminar air currents and other unwanted perturbations.

2. Optical alignment of the prototype telescope

The optical alignment of the prototype telescope was performed in a continuous-flow cleanroom environment. The environmental challenges, which include the coupling of vibrations and air turbulence to the interferometric wavefront tests, are usually addressed by temporarily turning off the cleanroom blowers. However, this option was not available due to the risk of contamination to the flight-certified room and associated equipment. Furthermore, the turning off the airflow in the room results in a significant temperature drifts with short time constants and large dependence on the outside air temperature—a factor which could also affect telescope wavefront measurements. Nevertheless, to the extent possible, many measures were taken to mitigate unwanted effects of turbulent air flow and acoustic vibrations common in such an environment. These measures include use of acoustic dampening padding on the walls and hard surfaces of the cleanroom, and placement of flat panels to adjust local airflow directions and thereby limit the effect of turbulence on the interferometry.

Figure 7 shows the setup used to achieve optical alignment of the prototype.

First, a large 18 inch flat auto-collimating flat (ACF) was placed unclamped on teflon supports in a strain-free mount and aligned to the primary mirror. To accomplish this task, a point source generated by a Point-Source-Microscope (PSM) was placed at the focus of the telescope primary mirror thereby overfilling the primary mirror. Due to the mounting structure of the secondary mirror intruding on the desired location of the PSM, a fold flat was placed at 45° in front of the secondary mirror. Fine adjusters on the ACF and PSM, in addition to course translation of the primary mirror mount, were then repeatedly used to firstly achieve a retro-reflection into the PSM off this fold flat, and secondly to minimize and center the return spot. With this relative alignment between the ACF and PSM now achieved, the primary mirror and ACF locations were locked down.

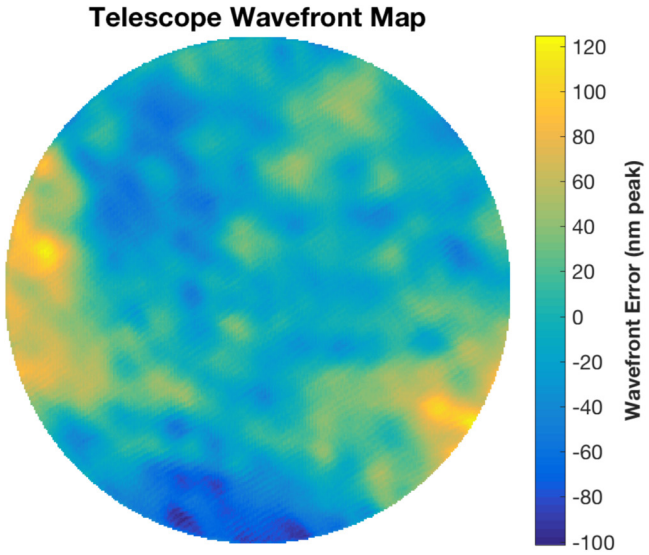

Figure 8. Wavefront map of the aligned telescope. The error was found to be 34.3 nm RMS.

Next the input beam angle was set by using a theodolite to orient the angle of a small flat relative to the ACF. This input beam flat (IBF) was placed very close to the location of the tertiary and quaternary mirrors. A laser unequal path interferometer (LUPI) [19] was then nulled off the IBF—thus ensuring the LUPI beam is at the nominal input beam angle of the optical design. The LUPI used was a Buccini Model MIC-1, mounted on positioning stage, allowing independent adjustments in five degree-of-freedom. Later in the process, this LUPI will be used to determine the telescope wavefront error by interfering the double-passed telescope wavefront with the internal reference pick-off of the LUPI instrument.

Subsequently, the tertiary and quaternary mirrors were placed into their holders and a delrin alignment spacer placed between them and bolted into place. This delrin block was precision-machined according to the optical prescription to have through holes at the correct locations and angles for the optical beam to be transmitted through. The LUPI was then translated to the input aperture of the telescope and it was verified that the beam transmits through the assembly of the delrin block and optical mirrors.

The secondary mirror was then placed into its holder, with the 45 degree fold mirror now removed. The secondary mirror was translated and tilted so that the beam from the tertiary mirror is reflected to and centered on the primary mirror, and retro-reflects off the ACF back through the telescope. Using iterative centration of the beam on the primary and alignment of the secondary, fringes were then observed on the LUPI camera and read out to a desktop computer. As is common in misaligned optical systems, there were initially a large number of fringes and a high degree of optical aberration.

The differential adjusters on the secondary mount were then adjusted to reduce the number of static fringes observed in the interferometric readout. Models of the optical system, implemented in Matlab, were used to determine which adjustment had the highest impact on the residual wavefront aberration. Similar models are discussed in more detail in [20]. Non-orthogonality of the physical adjustments could be incorporated into this model and thus lead to a more efficient alignment process—by indicating which adjuster, or sequence of adjusters, would produce a beneficial wavefront map change. The time-efficient alignment of several

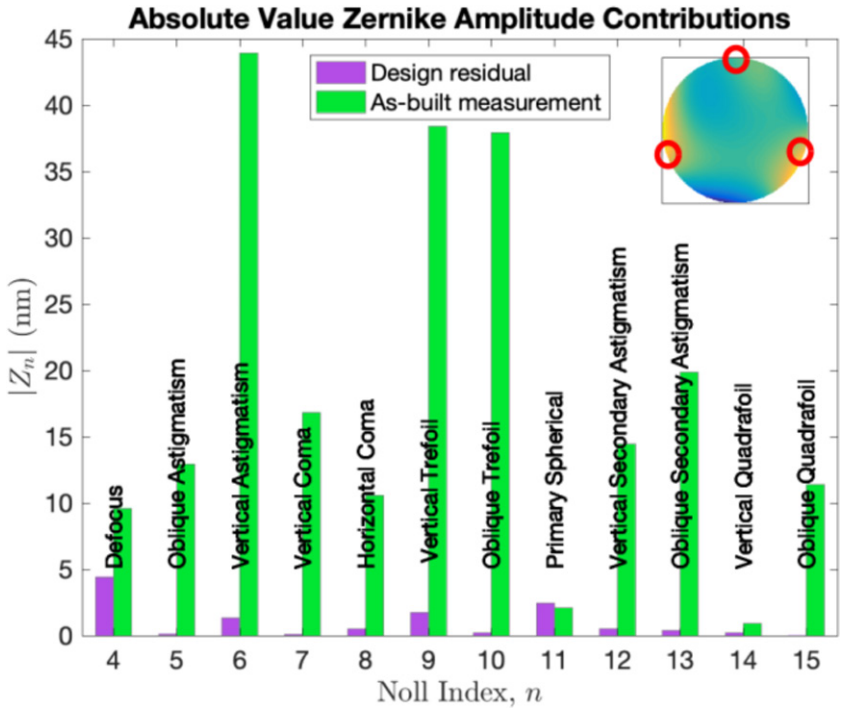

Figure 9. Decomposition of the wavefront maps into the first 15 Zernike components, for both the optical design residual and the as-built system. Mirror surface figure errors (sourced both by mounting and fabrication) as well as mirror alignment errors are the main contributions to the RMS wavefront error. The inset shows the re-composition of the as-built measurement, with red circles indicating the approximate location of the primary mirror mounting clips.

eventual flight telescopes is important for schedule control in LISA and this method was very useful in achieving alignment quickly.

Reducing the number of fringes through iterative alignment of the secondary resulted in a telescope wavefront error which was less than the specification of 35.5 nm. To calibrate the ACF, it was clocked in its mount in increments of 60° while observing the wavefront error in the double-pass test. This standard clocking procedure is usually used to alter the wavefront error contribution of the ACF while keeping the contribution from the telescope constant. However, in this case the clocking procedure produced no change in the overall wavefront—indicating that the ACF gave a negligible wavefront error contribution to the measurement. This fact was due mainly to the clamp-free mounting of the ACF along with its intrinsically low surface figure error.

3. Performance of the aligned system

The wavefront map of the aligned telescope is shown in figure 8. The telescope meets the wavefront error requirement of $\frac{\lambda}{30}$ at the 1064 nm laser wavelength, or approximately 35.5 nm. The measured wavefront map can be decomposed into its spatial frequency components. In this work, the low spatial frequency components are taken as the first fifteen Zernike components of the wavefront map. The residual, after removing these low spatial frequency components

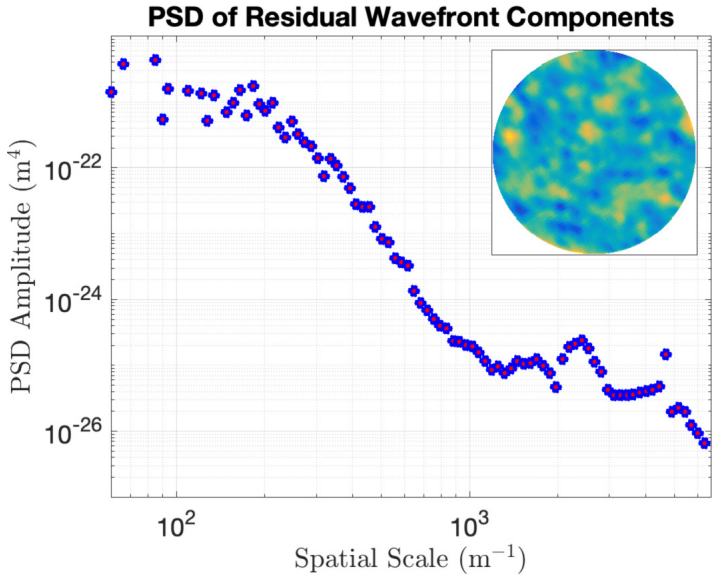

Figure 10. Power spectral density (PSD) of the residual wavefront components after removal of the first 15 Zernike components. The x-axis corresponds to 2π divided by the component length-scale. The inset shows ths residual wavefront error map, from which the PSD was computed. The variations in amplitudes of higher spatial frequency components (above approximately 10^3 m^{-1}) are likely artifacts of the measurement and data acquisition process.

from the measured map, is referred to as the mid and high spatial frequency components. We now discuss these different spatial frequency bands individually.

3.1. Low spatial frequency components

The Zernike components of the wavefront were fit and extracted. Figure 9 shows the decomposition of the measured and design wavefront error maps into the first fifteen Zernike amplitudes.

The clear hot-spots in the wavefront map corresponded in location roughly to the positions of three mounting clips for the telescope's primary mirror, highlighted by red circles in figure 9. These clips are thought to introduce trefoil into the primary mirror by surface deformation, which impacts the overall telescope optical performance. The other large contributors—the astigmatism components—are likely due to a small residual misalignment of the secondary mirror.

In some cases, the adjustment resolution of the secondary mirror limited the ability to further align out these wavefront aberration components. For example, the linear optical model was used to determine that a 1.5 μm translation in the telescope $\hat{y}$-axis coupled to a 255 μrad tilt about the $\hat{x}$-axis can reliably reproduce the observed astigmatism components. Taking into consideration this high sensitivity, as well as the non-orthogonality of the physical adjusters, achieving further deterministic suppression of individual Zernike terms is difficult and time-consuming beyond this level for the prototype. With less sensitive optical designs and better adjustment resolution, it is possible that such suppression can be reliably and repeatably achieved.

3.2. Mid and high spatial frequency components

After fitting and removing the first fifteen Zernike components, the remaining wavefront error is referred to as the residual wavefront error and is comprised of only mid and high spatial frequency components. Such components are unlikely to be sourced from optical misalignments and mount-induced mirror deformations, and instead originate from the fabrication techniques used to create the optics and from measurement artifacts. All grinding and polishing techniques unavoidably leave detectable figure errors on optics at these scales. Furthermore, another possible source of the detectable high spatial frequency wavefront errors are artifacts of the test interferometer, including undesirable ghost fringes and pixel crosstalk.

The mid and high spatial frequency components of a residual wavefront error map are often characterized by a power spectral density (PSD) [21, 22]. Procedures for calculating the PSD from optical surface or wavefront data are detailed in [22, 23]. Analyzing the residual wavefront map of the prototype telescope results in the power spectral density of residual wavefront error shown in figure 10. It should be noted that the power spectral density is also often used to represent surface errors on mirror topography measurements, but in this case has been applied to the residual wavefront error in large beam space.

The RMS contribution of these mid and high spatial frequency components can also be determined by integration of the power spectral density. Integrated over all measured frequencies, this RMS contribution was found to be 16.6 nm RMS for the residual wavefront map shown. This contribution signifies that if mount-induced, gravity-induced and alignment-induced errors could be sufficiently mitigated in a future LISA telescope, optical mirror fabrication at the level of that performed for the prototype would enable less than 20 nm of wavefront error. Note, however, that the mitigation of these low spatial frequency components requires careful mechanical design including the modeling of mount-induced and gravity-induced errors, and the ability to place optics with very high positioning resolution. Complementary alternative techniques may also need to be considered.

The high spatial frequency components have an impact on the backscattered light performance of the telescope rather than the wavefront error. Therefore the drivers of those high spatial frequency requirements have been derived from the scattered light requirements and will be addressed in more detail in subsequent works.

4. Conclusion

A prototype telescope for the LISA mission has been designed and fabricated. Key features of the build include allocating surface figure errors to individual components, as well as allowing margin for alignment errors and testing imprecision. A linear optical model formalism was implemented for aid in aligning the telescope based on the sensitivities of mirror positioning and will enable more efficient alignment of future flight telescopes. Furthermore, using these techniques, the prototype was aligned to meet the present mission-driven RMS wavefront error allocation of $\frac{\lambda}{30}$, corresponding to less than 35.5 nm RMS. A full characterization of the optical performance was performed, including low, mid and high spatial frequency contributions. Possible avenues of future research include investigations of polarization effects, pupil placements, wavefront composition constraints, backscattering and dimensional stability, as well as the ability to predict and account for any ground-to-orbit changes. Several of these properties are best investigated in a more flight-like prototype LISA telescope unit.

Acknowledgments

We wish to acknowledge the invaluable work of the NASA Goddard Optics Branch, particularly the optical design group—Garrett West (NASA) was key in developing the optical prescription for the prototype and Joseph Howard (NASA) was instrumental in the development of the formalism of the linear optical model which aided greatly in the alignment phase. We also specifically thank Peter Blake (NASA, retired) for his invaluable assistance in aligning the prototype telescope and for helping to implement many metrology techniques used in this work. We also thank GSFC colleagues Kevin Miller (NASA) and Edward Bragg (Stinger Ghaffarian Technologies) for spectrophotometer measurements of coatings. We acknowledge the invaluable assistance of the many students who participated in the clean-room laboratory work, particularly Hudson Loughlin (Princeton), Julie Rose (University of Maryland) and Lea Bischoff (Max Planck Institute for Gravitational Physics—Albert Einstein Institute in Hannover). We also thank Jim Burge, Benjamin Lewis, Marty Valente and Kevin Harris (Arizona Optical Systems) for design and construction of the metering structure and mounts, for help integrating and aligning the optics and, more generally, for many fruitful discussions.

Finally, the authors gratefully acknowledge that much of this work was supported by NASA through the CRESST Cooperative Agreement under award number 80GSFC17M0002, as well as through the Strategic Astrophysics Technology Program under an award for 14-SAT14-0014.

ORCID iDs

Shannon R Sankar https://orcid.org/0000-0002-1740-0532

References

[1] Abbott B P *et al* 2016 Observation of gravitational waves from a binary black hole merger *Phys. Rev. Lett.* **116** 061102
[2] Abbott B P *et al* 2017 Gw170817: observation of gravitational waves from a binary neutron star inspiral *Phys. Rev. Lett.* **119** 161101
[3] Danzmann K *et al* 2017 LISA Laser interferometer space antenna—a proposal in response to the ESA call for L3 mission concepts (arXiv:1702.00786)
[4] Hughes S A 2006 A brief survey of LISA sources and science *AIP Conf. Proc.* **873** 13–20
[5] Science Study Team 2018 LISA Science requirements document https://www.cosmos.esa.int/documents/678316/1700384/SciRD.pdf (Accessed: 20 August 2019)
[6] Miller M C 2009 Intermediate-mass black holes as LISA sources *Class. Quantum Grav.* **26** 094031
[7] Gair J R, Barack L, Creighton T, Cutler C, Larson S L, Phinney E S and Vallisneri M 2004 Event rate estimates for LISA extreme mass ratio capture sources *Class. Quantum Grav.* **21** S1595
[8] Berti E 2006 LISA observations of massive black hole mergers: event rates and issues in waveform modelling *Class. Quantum Grav.* **23** S785
[9] Cornish N J and Porter E K 2006 MCMC exploration of supermassive black hole binary inspirals *Class. Quantum Grav.* **23** S761
[10] Livas J C, Arsenovic P, Crow J A, Hill P C, Howard J M, Seals L T and Shiri S 2013 Telescopes for space-based gravitational wave missions *Opt. Eng.* **52** 091811
[11] Sankar S R and Livas J C 2014 Optical telescope design for a space-based gravitational-wave mission *Proc. SPIE* **9143** 914314
[12] Caldwell M, McNamara P and Glennmar A 1998 Optical engineering requirements for the LISA wavefront error budget *AIP Conf. Proc.* **456** 156–64
[13] Bender P L 2005 Wavefront distortion and beam pointing for LISA *Class. Quantum Grav.* **22** S339

[14] Sasso C, Mana G and Mottini S 2018 Coupling of wavefront errors and jitter in the LISA interferometer: far-field propagation *Class. Quantum Grav.* **35** 185013
[15] Sasso C, Mana G and Mottini S 2018 Coupling of wavefront errors and pointing jitter in the LISA interferometer: misalignment of the interfering wavefronts *Class. Quantum Grav.* **35** 245002
[16] Vinet J-Y, Christensen N, Dinu-Jaeger N, Lintz M, Man N and Pichot M 2019 LISA Telescope: phase noise due to pointing Jitter *Class. Quantum Grav.* **36** 205003
[17] Hammesfahr A *et al* 2000 LISA—Study of the Laser Interferometer Space Antenna, Final *Technical Report ESA* Industrial Study at Phase A, ESTEC Contract no 1363 1/99/NL/MS, DSS Report No LI-RP-DS-009 (Friedrichshafen, Germany: Dornier Satellitensysteme Gmbh)
[18] Elliffe E J *et al* 2005 Hydroxide-catalysis bonding for stable optical systems for space *Class. Quantum Grav.* **22** S257
[19] Houston J, Buccini C and O'Neill P 1967 A laser unequal path interferometer for the optical shop *Appl. Opt.* **6** 1237–42
[20] Howard J M 2004 Optical modeling activities for the James Webb space telescope (JWST) project: I. The linear optical model *Proc. SPIE* **5178**
[21] Walsh C J, Leistner A J and Oreb B F 1999 Power spectral density analysis of optical substrates for gravitational-wave interferometry *Appl. Opt.* **38** 4790–801
[22] Elson J M and Bennett J M 1995 Calculation of the power spectral density from surface profile data *Appl. Opt.* **34** 201–8
[23] Sidick E 2009 Power spectral density specification and analysis of large optical surfaces *Proc. SPIE* **7390** 73900L